Source of Acquisition
NASA Marshall Space Flight Center

Self–consistent model of magnetospheric ring current and propagating electromagnetic ion cyclotron waves. 2. Wave induced ring current precipitation and thermal electron heating

G. V. Khazanov

NASA, Marshall Space Flight Center, Huntsville, Alabama, USA

K. V. Gamayunov

NASA, Marshall Space Flight Center, Huntsville, Alabama, USA

D. L. Gallagher

NASA, Marshall Space Flight Center, Huntsville, Alabama, USA

M. W. Liemohn

Space Physics Research Laboratory, University of Michigan, Ann Arbor, Michigan, USA

J. U. Kozyra

Space Physics Research Laboratory, University of Michigan, Ann Arbor, Michigan, USA

Short title: RC–EMIC WAVE–RAY TRACING MODEL, 2

Abstract. This paper continues presentation and discussion of the results from our new global self–consistent theoretical model of interacting ring current ions and propagating electromagnetic ion cyclotron waves [*Khazanov et al.,* 2006]. To study the effects of electromagnetic ion cyclotron wave propagation and refraction on the wave induced ring current precipitation and heating of the thermal plasmaspheric electrons, we simulate the May 1998 storm. The main findings after a simulation can be summarized as follows. Firstly, the wave induced ring current precipitation exhibits quite a lot of fine structure, and is highly organized by location of the plasmapause gradient. The strongest fluxes of about $4 \cdot 10^6$ $(\mathrm{cm} \cdot \mathrm{s} \cdot \mathrm{sr})^{-1}$ are observed during the main and early recovery phases of the storm. The very interesting and probably more important finding is that in a number of cases the most intense precipitating fluxes are not connected to the most intense waves in simple manner. The characteristics of the wave power spectral density distribution over the wave normal angle are extremely crucial for the effectiveness of the ring current ion scattering. Secondly, comparison of the global proton precipitating patterns with the results from RAM [*Kozyra et al.,* 1997a] reveals that although we observe a qualitative agreement between the localizations of the wave induced precipitations in the models, there is no quantitative agreement between the magnitudes of the fluxes. The quantitative differences are mainly due to a qualitative difference between the characteristics of the wave power spectral density distributions over the wave normal angle in RAM and in our model. Thirdly, the heat fluxes to plasmaspheric electrons caused by Landau resonate energy absorption from electromagnetic ion cyclotron waves are observed in the postnoon–premidnight

MLT sector, and can reach the magnitude of 10^{11} eV/(cm$^2 \cdot$ s). The Coulomb energy degradation of the RC H^+ and O^+ ions maximizes at about 10^{11} (eV/(cm$^2 \cdot$ s), and typically leads to electron energy deposition rates of about $2 \cdot 10^{10}$ (eV/(cm$^2 \cdot$ s) which are observed during two periods; 32–48 hours, and 76–86 hours after 1 May, 0000 UT. The theoretically derived spatial structure of the thermal electron heating caused by interaction of the ring current with the plasmasphere is strongly supported by concurrent and conjugate plasma measurements from the plasmasphere, ring current, and topside ionosphere [*Gurgiolo et al.*, 2005]. Finally, the wave induced intense electron heating has a structure of the spot–like patches along the most enhanced density gradients in the plasmasphere boundary layer and can be a possible driver to the observed but still not explained small–scale structures of enhanced emissions in the stable auroral red arcs.

1. Introduction

This study continues presentation and discussion of the results of a simulation based on a new global self–consistent theoretical model of interacting ring current (RC) ions and propagating electromagnetic ion cyclotron (EMIC) waves [*Khazanov et al.,* 2006; here referred to as paper 1]. All the details regarding this model can be found in paper 1. Briefly, this is the further development of the self–consistent theoretical model of *Khazanov et al.* [2002; 2003], and in comparison with the earlier model, this new model explicitly includes the EMIC wave propagation and refraction in a multi–ion magnetospheric plasma, and a general form of the wave kinetic equation is used in order to describe the wave evolution.

One of the most important consequences of the RC–EMIC wave interaction is a scattering of the RC ions into the loss cone. This process leads to decay of the RC [see, e. g., *Cornwall et al.,* 1970], especially during the main phases of the storms when the RC decay time of about one hour or less is possible [*Gonzalez et al.,* 1989]. It follows from a comparison presented in paper 1 that although the ring current–atmosphere interaction model (RAM) of *Kozyra et al.* [1997a] and *Jordanova et al.* [1997; 2001] takes into account some features of the EMIC wave propagation and refraction, their RAM predicts the more extended and less intense equatorial EMIC wave distributions in comparison with the results from our model (for details of the comparison see paper 1). So we are required now to consider in detail how the above differences impact the RC ion precipitation, and to compare the global RC proton precipitating patterns produced

by this version of RAM and by our model. This comparison is presented in Section 2 along with a discussion of the main reason for the differences found between these two simulation result sets.

The overlap of the RC with the outer plasmasphere plays a major role in the storm–time related electron temperature elevations in the subauroral topside ionosphere. This temperature enhancement affects the density and composition of the upper ionosphere and thermosphere. One of the major deficiencies in the study of the coupling of the RC to the ionosphere is the lack of concurrent and conjugate magnetospheric and ionospheric plasma measurements over complete anomalous heating events. Recently, *Gurgiolo et al.* [2005] have presented a global view of the RC–plasmasphere system during the 18–19 June 2001 storm. In order to have concurrent and conjugate plasma measurements from the plasmasphere, the RC, and the topside ionosphere these authors have combined data from the IMAGE and DMSP satellites. IMAGE has been used to obtain the plasmaspheric He^+ ion density in the geomagnetic equatorial plane (from the Extreme UltraViolet imager, EUV), and to obtain global 2D distributions of the RC ion fluxes in the geomagnetic equatorial plane (from both the High and Medium Energy Neutral Atom imagers, HENA and MENA). DMSP (F–12, F–13, and F–15) satellites have been used to obtain electron temperature and precipitating electron and ion fluxes along the satellite tracks at a nominal altitude of 830 km. *Gurgiolo et al.* [2005] have analyzed the relationships of the topside heating of the subauroral ambient electrons with the plasmasphere and RC conditions. They have found that subauroral heating occurs within the plasmasphere–RC overlap region, and can be separated into

two classifications; inner and outer heating events. The inner events take place well earthward of the plasmapause ($> 0.75R_E$ in the equatorial plane) and generally occur in the dawn MLT sector. The outer events occur in the plasmasphere boundary layer within $0.75R_E$ of the equatorial plasmapause, and are more prevalent in the dusk MLT sector.

In order to associate our theoretical results with the observations of *Gurgiolo et al.* [2005], in Section 3 we calculate and present the energy depositions to the thermal plasmaspheric electrons from two energy sources; the EMIC wave energy absorption due to Landau resonance with electrons, and the Coulomb energy degradation of the RC H^+ and O^+ ions. A possible relationship of the wave induced heating structure to the spot–like patches of enhanced emissions inside of the stable auroral red (SAR) arcs is also discussed in Section 3. Section 4 briefly summarizes the crucial features of the developed RC–EMIC wave model, and lists the main findings of paper 2.

2. Wave Induced Precipitation of Ring Current Ions

One of the most pronounced manifestations of the RC–EMIC wave interaction is a scattering of the RC ions into the loss cone. This process leads to decay of the RC [see, e. g., *Cornwall et al.,* 1970], especially during the main phases of the storms when the RC decay time of about one hour or less is possible [*Gonzalez et al.,* 1989]. In order to demonstrate further the role of the EMIC wave propagation and refraction, we obtain

a global history of the RC proton precipitating flux,

$$J_{lc} = \frac{1}{\Omega_{lc}} \int_{E_1}^{E_2} \mathrm{d}E \int_{\mu_{lc}}^{1} \mathrm{d}\mu_0 j, \quad \Omega_{lc} = \int_{\mu_{lc}}^{1} \mathrm{d}\mu_0, \tag{1}$$

for the May 1998 storm. In equation (1), μ_{lc} is the cosine of the equatorial pitch angle at the boundary of loss cone, and j is the equatorial ion differential flux. For the presentation below, we selected exactly the same time intervals as in paper 1; the first interval takes place on 2 May, from 24 hours to 48 hours after 1 May, 0000 UT, and the second interval is from 72 hours to 86 hours after 1 May, 0000 UT. For reference purposes we first present the results from the model with no wave–particle interaction (original version of RAM, see paper 1). In Figure 1 we show the selected snapshots of the precipitating fluxes integrated over energy range $1 - 50$ keV. These fluxes are resulted only from magnetospheric convection of the RC ions and its scattering due to Coulomb collisions with thermal plasma. The most intense precipitating fluxes do not exceed 10^6 $(\mathrm{cm} \cdot \mathrm{s} \cdot \mathrm{sr})^{-1}$, and are observed in the postmidnight–dawn MLT sector for $L > 4.25$ during the early recovery phase, starting at 80 hours after 1 May, 0000 UT.

Figure 1

The precipitating fluxes obtained from a simulation based on the system of governing equations derived in paper 1 (see equations (21) and (22) in paper 1) are presented in Figure 2. First of all, we observe that the wave induced precipitating fluxes exhibit quite a lot of fine structure, and are highly organized by location of the plasmapause gradient (compare with the equatorial wave distributions in Figure 6 of paper 1). In agreement with previous modeling results [*Jordanova et al.,* 2001], the wave induced precipitating fluxes are more intense in comparison with the results in

Figure 2

Figure 1, and the strongest fluxes of about $4 \cdot 10^6$ $(\mathrm{cm} \cdot \mathrm{s} \cdot \mathrm{sr})^{-1}$ are observed during the main and early recovery phases of the storm. The very interesting and probably more important conclusion can be derived by comparing Figure 2 with Figure 6 in paper 1; in a number of cases the most intense precipitating fluxes are not simply connected to the most intense EMIC waves. For example, the strongest precipitating flux of $4 \cdot 10^6$ $(\mathrm{cm} \cdot \mathrm{s} \cdot \mathrm{sr})^{-1}$ is observed at L=5.25, MLT=16 at 86 hours after 1 May, 0000 UT, but there is quite moderate EMIC wave intensity of only $B_{\mathrm{w}}^2 = 2.7$ nT^2.

Let us consider this feature in detail by analyzing the data from three (MLT, L–shell) points in snapshot at 48 hours; point (a) L=5.25, MLT=16, point (b) L=5.75, MLT=15, and point (c) L=5.75, MLT=14. The precipitating fluxes and the EMIC wave power densities in these points are listed in Table 1 in the "Our Model" columns. (Note that the extra numbers provided in Table 1 will be used later, and below we use the subscripts (a), (b), and (c) in order to refer to the points (a), (b), and (c), respectively.) The number densities for the $1-50$ keV range RC protons are practically the same in all these points, and they are in a range $1.1-1.4$ cm^{-3}. So the observed differences between precipitating fluxes are mainly due to differences in the RC–EMIC wave diffusion rates which depend on the EMIC wave power spectral density. The simple analysis of the magnitudes of the precipitating fluxes and the EMIC wave intensities can not explain these differences; for example, $B_{\mathrm{w,(a)}}/B_{\mathrm{w,(c)}} = 1.3$ and $J_{lc,\mathrm{(a)}}/J_{lc,\mathrm{(c)}} = 17.7$, but on the other hand the ratio $B_{\mathrm{w,(b)}}/B_{\mathrm{w,(a)}} = 1.2$ is practically the same as $B_{\mathrm{w,(a)}}/B_{\mathrm{w,(c)}}$ but $J_{lc,\mathrm{(b)}}/J_{lc,\mathrm{(a)}} = 0.4$ is far less than 1. At the same time, as we have demonstrated in paper 1 (see Figure 9 in paper 1), the EMIC wave power spectral density distributions

Table 1

over the equatorial wave normal angle are essentially different for cases (a), (b), and (c). In case (a), the EMIC wave energy is entirely concentrated in the region of generation, i. e. in the region of small θ_0. As a consequence, we observe the most intense RC proton precipitating fluxes (the EMIC wave growth rates are maximized for a field–aligned wave propagation that is caused by most efficient wave–particle interaction). In case (c), however, because the wave energy is in the region of large θ_0 only, the smallest RC precipitating fluxes are produced. In the intermediate case (b), while the wave power $B^2_{w,(b)}$ has the greatest amplitude, only the wave energy concentrated in a quasi field–aligned region can effectively scatter the RC protons, and we compute a flux that is more than twice less than in case (a). So the characteristic of the EMIC wave power spectral density distribution over θ_0 is an extremely crucial factor for the effectiveness of the RC ion scattering.

In paper 1 we have compared the global He^+–mode energy distributions derived from our new model with the results of other RAM–based global model where the different EMIC wave description has been adopted [*Kozyra et al.,* 1997a; *Jordanova et al.,* 1997; 2001]. Let us further continue a comparison and present the RC proton precipitating fluxes which are obtained from a simulation with employing this earlier version of RAM. The results of this simulation are presented in Figure 3. We have demonstrated in paper 1 that EMIC wave growth is only slightly controlled by plasmapause location in the version of RAM by *Kozyra et al.* [1997a], and that the equatorial energy distributions of generated waves are more extended and more smooth in comparison with our results, at least during the May 1998 storm period (compare

Figure 3

Figures 6 and 8 in paper 1). As a consequence, the (MLT, L–shell) distributions of the wave induced precipitating fluxes are also more smooth and more extended in Figure 3 compare to Figure 2. Although we observe a qualitative agreement between localizations of the enhanced fluxes in Figures 2 and 3, there is no quantitative agreement between the magnitudes of these fluxes. As we have found in paper 1, in general this version of RAM [*Kozyra et al.,* 1997a; *Jordanova et al.,* 1997] produces less intense equatorial wave distributions during the May 1998 storm period. At the same time, the wave induced precipitating fluxes in Figure 3 are essentially more intense than in Figure 2, and reach the magnitude of $3.5 \cdot 10^7$ $(\mathrm{cm} \cdot \mathrm{s} \cdot \mathrm{sr})^{-1}$ at L=4.25, MLT=19 at 32 hour after 1 May, 0000 UT.

Selecting the same spatial points (a), (b) and (c) as we did above in analyzing Figure 2, we can obtain the RC proton precipitating fluxes and the EMIC wave power densities from Figure 3 and Figure 8 in paper 1. All these numbers are presented in Table 1 in the "RAM" columns. Above, analyzing Figure 2, we showed that the effectiveness of the RC ion scattering by EMIC waves dramatically depends on the wave power spectral density distribution over θ_0. In the version of RAM under comparison, *Kozyra et al.* [1997a] (see also *Jordanova et al.* [1997, 2001]) have used a quasi field–aligned power spectral density distribution with wave normal angle which is a Gaussian distribution in the region of $0 < \theta_0 < \pi/4$ with maximum at $\theta_0 = 0$. It follows from Figure 9(a) in paper 1 that the EMIC wave energy is entirely concentrated in the region of $0° < \theta_0 < 50°$ in spatial point (a). Although these power spectral density distributions do not appear as Gaussian functions, the wave energy is observed

practically in the same wave normal angle region as it has been set by *Kozyra et al.* [1997a] and *Jordanova et al.* [1997; 2001].

According to *Kennel and Petschek* [1966], the steady state wave induced diffusion strength is scaled by factor $z_0 = \alpha_0/\sqrt{D\tau_{atm}}$, where α_0 is the pitch–angle boundary of the loss cone, D is a pitch–angle diffusion coefficient which depends on the EMIC wave power spectral density, and τ_{atm} is a typical time for leakage of the RC ions into the atmosphere. Assuming that the wave power spectral densities from our model and from the model of *Kozyra et al.* [1997a] have the same shapes in point (a), we can compare only the wave intensities from these two models. So in order to relate the magnitudes of precipitating fluxes in point (a) from Figures 3 and 2, we need to re–normalize one flux accordingly to a ratio of the wave intensities from these two global models; $2.5 \cdot 10^6\ (\mathrm{cm} \cdot \mathrm{s} \cdot \mathrm{sr})^{-1} \times \sqrt{0.2/28.6} = 2.1 \cdot 10^5\ (\mathrm{cm} \cdot \mathrm{s} \cdot \mathrm{sr})^{-1}$. This estimation is very close to a magnitude of precipitating flux from Figures 3, $J_{lc,(\mathrm{a})} = 2.7 \cdot 10^5\ (\mathrm{cm} \cdot \mathrm{s} \cdot \mathrm{sr})^{-1}$.

The wave power spectral density distributions in points (b) and (c) are absolutely not quasi field–aligned, and we can not use the above simple procedure in these points in order to relate the precipitating fluxes from Figure 2 with the results from Figure 3. At the same time, we see that EMIC wave intensities from the model of *Kozyra et al.* [1997a] are at least five times less in these spatial points than in our model (see Table 1). On the other hand, the precipitating fluxes in Figure 3 are at least four times greater than in Figure 2. So we believe that the observed differences in magnitudes of the wave induced proton precipitating fluxes in points (b) and (c) from Figures 2 and 3 are mainly due to a qualitative difference between the characteristics of the

EMIC wave power spectral density distributions over θ_0. The resulting power spectral density distributions in our model are self–consistently determined by evolution of the RC–EMIC wave system itself. As we have shown in paper 1, all these distributions are not Gaussian distributions, and as we can see, the most important is that EMIC wave energy can occupy not only the region of generation, but the entire wave normal angle region and even the region near $\theta_0 = \pi/2$ only. On the other hand, *Kozyra et al.* [1997a] have used a quasi field–aligned power spectral density distribution that is not always a good fit to the actual form of the distribution over wave normal angle.

It is very clear demonstrated above that the EMIC wave power spectral density distribution over the wave normal angle can extremely impact the effectiveness of the RC ion scattering. At the same time, we considered only three spatial points in one snapshot, and it as very interesting now to see the wave power spectral density distributions on the global spatial and temporal scales. In order to provide such global view we consider the following ratio,

$$As = \frac{\int_{\omega_{min}}^{\omega_{max}} \mathrm{d}\omega \left(\int_{\pi/4}^{\pi/2} \mathrm{d}\theta_0 B^2(\omega, \theta_0) - \int_0^{\pi/4} \mathrm{d}\theta_0 B^2(\omega, \theta_0) \right)}{\int_{\omega_{min}}^{\omega_{max}} \mathrm{d}\omega \int_0^{\pi/2} \mathrm{d}\theta_0 B^2(\omega, \theta_0)}, \qquad (2)$$

where $B^2(\omega, \theta_0)$ is a square of the equatorial spectral magnetic field of the He^+–mode of EMIC waves, ω and θ_0 are the wave frequency and the equatorial wave normal angle, respectively. The ratio As is in a range [-1, 1] and characterizes the wave power spectral density asymmetry over wave normal angle; $As = -1$ if the wave energy is entirely concentrated in the range $0 \leq \theta_0 \leq \pi/4$, and $As = 1$ if the wave energy is in the range $\pi/4 < \theta_0 \leq \pi/2$ only. Figure 4 demonstrates the calculated EMIC wave power spectral

Figure 4

density asymmetry at the selected snapshots during the May 1998 storm. The quasi field–aligned, highly oblique, and intermediate wave distributions are represented in the spectrograms. So all not quasi field–aligned distributions shown in Figure 9 of paper 1 are not unusual distributions and are widely observed in the results of our simulation.

3. Heating of Thermal Plasmaspheric Electrons and Subauroral Ionospheric Temperature Enhancement

3.1. EMIC Wave and Coulomb Heating of Thermal Plasmaspheric Electrons

The EMIC waves generated by the RC ions not only cause the RC ion scattering into the loss cone but also effectively transfer energy to thermal plasmaspheric electrons due to resonant Landau damping. The total energy deposition rate to the thermal electrons can be obtained by integrating the local EMIC wave energy deposition rate along each geomagnetic field line from the equator to the ionosphere altitude. Assuming no other energy sources or sinks exist along the geomagnetic field line above the ionosphere, the resulting heat flux at the ionospheric level can be calculated as

$$P_{\mathrm{w},e} = -B_{\mathrm{iono}} \int_0^{s_1} \frac{\mathrm{d}s}{B(s)} \int_{\omega_1}^{\omega_2} \mathrm{d}\omega \int_0^{\pi} \mathrm{d}\theta \frac{B^2(\omega,\theta,s)}{4\pi} \gamma_e(\omega,\theta,s) . \tag{3}$$

In equation (3), s is a coordinate along geomagnetic field line, θ is the wave normal angle, $B^2(\omega,\theta,s)$ is the squared spectral magnetic field of the He^+–mode of EMIC waves, $\gamma_e(\omega,\theta,s)$ is the Landau damping rate of the He^+–mode of EMIC waves due to interaction with thermal plasmaspheric electrons, and the ratio of geomagnetic field amplitudes at the ionosphere altitude and at the current position, $B_{\mathrm{iono}}/B(s)$, takes

into account the change in the magnetic tube cross section along the field line. The Landau damping rate strongly depends on the the wave normal angle, and it is very sensitive to the ratio of the parallel phase velocity to the electron thermal velocity. The dependencies of the Landau damping rate on the wave normal angle are presented in Figure 5 for different sets of the plasma parameters. In order to calculate these damping rates we assume the plasma consists of the Maxwellian electrons, and cold ions; 77% of H^+, 20% of He^+, and 3% of O^+. Although the Landau damping rate does not equal to zero for small wave normal angles, it takes the reasonable values for highly oblique wave propagations only, and we provide in Figure 5 the wave normal angle ranges only where $|\gamma_e|/\omega \geq 10^{-4}$. The parallel phase velocity for the He^+–mode of EMIC waves is very close to Alfvén velocity which is $v_A = 4.4 \cdot 10^7$ cm/s for the case (a/b) in Figure 5. On the other hand, the damping rate maximizes for the ratio of the parallel phase velocity to the electron thermal velocity of about 1.2, i. e., $v_A/v_{T_e} = 1.2$ [see, e. g., *Cornwall et al.,* 1971]. This number corresponds to the electron temperature $T_e = 0.4$ eV, and we observe that Landau damping rate in Figure 5b is maximal for $T_e = 0.5$ eV (not shown damping rate for $T_e = 0.4$ eV only slightly exceeds the rate for $T_e = 0.5$ eV at its maximum). The further electron temperature increase leads to a power decrease of the damping rate. In the opposite case, when $v_A/v_{T_e} >> 1.2$, the Landau damping rate decreases exponentially. Note that all the results in Figures 5(c/d) and 5(e/f) can be understood if just keep in mind that $v_A \sim B/\sqrt{n_e}$.

Figure 5

The thermal plasmaspheric plasma in the present study is treated independently from a self–consistent dynamic of the RC–EMIC wave system (for details about the

core plasma density model, see paper 1). It means, particularly, that we do not take into account a change of the back–ground electron temperature due to resonant Landau damping of the EMIC waves. In order to check the sensitivity of the "wave" energy deposition rate to this restriction, we have made four runs with four different thermal electron temperatures of 0.5, 1.0, 2.0, and 5.0 electron volts. On the whole, the energy deposition rate is maximized for electron temperatures in the range of 1–2 eV, and less intense for the case of $T_e = 0.5$ eV than for $T_e = 5.0$ eV. Considering the global EMIC wave energy distribution, wave induced RC precipitating flux, and energy deposition rate, we did not find any essential differences between these four cases, and the "wave" energy deposition rate presented below will relate to the case of $T_e = 1$ eV.

For reference and comparison purposes, we also calculate the energy deposition rate to the thermal electrons due to Coulomb collisions with RC ions. According to *Young et al.* [1982], the total ion flux, measured at geostationary orbit, can be divided between the RC H^+, O^+, and He^+ depending on geomagnetic and solar activity as it is measured by Kp and $F_{10.7}$ indices. For the May 2–7, 1998 storm period the geosynchronous ion fractions are shown in Figure 6. The RC He^+ fraction does not exceed 4 % during this event, and the RC O^+ ions mostly populate $20 - 40$ % of the RC content. The latter allows us to assume that the RC is entirely made up of energetic H^+ and O^+ ions, and to ignore the RC He^+ in calculation of the Coulomb collision energy deposition rate to the thermal electrons. The energy deposition rate to the thermal electrons due to Coulomb interaction with the RC ions can be written in the same manner as equation (3). Considering the RC H^+ and O^+, multiplying their Coulomb drag energy loss

Figure 6

terms by the energy, and integrating over the entire phase space volume and along the geomagnetic field line, we get

$$\begin{aligned} P_{RC,e} &= -B_{\text{iono}} \int_0^{s_1} \frac{\mathrm{d}s}{B(s)} \int \mathrm{d}\mathbf{p} E \left(\frac{\delta F}{\delta t} \right)_{RC,e} \\ &= \int_0^{s_1} \mathrm{d}s \int \mathrm{d}E \cdot G \cdot \overline{j}, \quad RC = H^+, O^+, \end{aligned} \tag{4}$$

where an explicit form for the term $(\delta F/\delta t)_{RC,e}$ can be found, e. g., in *Khazanov et al.* [2003], $\overline{j}$ is the omnidirectional flux of the RC ions, and G is the Coulomb collisional energy loss per unit length experienced by the selected RC ion in a specified background plasma.

Figure 7 and Figure 8 demonstrate the temperature dependencies of the energy deposition rates to the thermal plasmaspheric electrons due to Coulomb collisions with the RC H^+ and O^+ during a period of the largest Dst minimum on 4 May, 1998. In order to present data in the same format as we did above (and also in paper 1), all the topside ionospheric heat fluxes are mapped back into the equatorial plane along the dipole field lines. The first, second, and third rows in these figures represent the results for the electron temperature of 0.5, 1.0, and 2.0 eV, respectively. As we can see from these figures, although the RC H^+ energy deposition rate dominates the RC O^+ energy source for the 1 and 2 eV electron temperatures, the H^+ energy source growths gradually with decrease of the electron temperature while the O^+ energy source increases much steeper for $T_e = 0.5$ eV. As a result, the O^+ energy source becomes greater then the H^+ source for 0.5 eV; actually, the RC O^+ energy deposition rate dominates the RC H^+ energy source mostly during the period presented in Figures 7

Figure 7
Figure 8

and 8 only, when the RC O^+ fraction growths substantially (see Figure 6).

In order to qualitatively understand the above dependencies of the collisional energy deposition rates on electron temperature let us consider function G introduced in equation (4). The results of calculation of the Coulomb collisional energy losses per unit length are presented in Figure 9 for both the RC H^+ and O^+, and for 0.5, 1, and 2 eV back-ground electron temperatures (the unit for G is not specified). Two vertical lines in Figure 9 restrict the typical energy range of maximum RC fluxes. We can see from Figure 9(a) that function G only slightly growths inside of the specified $10 - 100$ keV energy range with decrease of T_e. As a results, the energy deposition rate in Figure 7 growths gradually with temperature decrease. Comparing Figures 9(a) and 9(b) we see that inside of the $10 - 100$ keV energy range the function G for the RC O^+ not only growths faster with temperature decrease, but also dominates the corresponding values of the function G for the RC H^+ for all electron temperatures. In spite of the latter, there is not enough O^+ ions in the RC content, and the O^+ energy deposition rate in Figure 8 becomes greater then the H^+ source during a period of the largest Dst minimum only (in other words, growth of the O^+ fraction in the RC) and for $T_e = 0.5$ eV.

Figure 9

As we demonstrated above, both the "wave" and the Coulomb collisional energy sources for the thermal plasmaspheric electrons depend on electron temperature; the wave induced energy deposition rate is maximized for electron temperatures in the range of 1–2 eV, collisional energy source has a maximum for electron temperature of about 0.5 eV, and both these energy sources gradually decrease with further temperature

enhancement. At the same time, we treat thermal plasma not self–consistently in the present study, i. e., we do not take into account a change of the back–ground electron temperature due to interaction with waves and RC. So we have to specify the electron temperature in order to compare the "wave" and "collisional" energy sources. Because of the Coulomb collisional energy source can readily act as the primer to heat plasmaspheric electrons [*Thorne and Horne,* 1992; *Kozyra et al.,* 1987] below we use $T_e = 1$ eV as an electron temperature. Selecting the same time cuts as we did in Section 2, we first present in Figure 10 the Coulomb collisional energy deposition rates separately for the RC H^+ and O^+ ions for the case $T_e = 1$ eV. The first and the second rows in Figure 10 represent the O^+ energy deposition rate, and the third and the fourth ones are the energy source resulting from the RC H^+, respectively. The white lines in the figure are the contours of equatorial plasmaspheric electron density. The most intense energy depositions for both RC ions are localized well earthward of the plasmapause, and the H^+ energy source is a little more powerful then the O^+ energy source. Note that for the RC H^+ ions, the greatest energy deposition rate of about 10^{11} (eV/(cm$^2 \cdot$ s) is observed at hour 40 and it is due to the RC protons with energy below 1 keV, and the "belts" of the enhanced depositions outside of the plasmapause are due to the protons with energy in a range $\sim 10 - 100$ eV.

Figure 10

From the same simulation, based on the system of governing equations derived in paper 1, we obtained the energy deposition rates to the thermal plasmaspheric electrons as they described by equations (3) and (4). The selected snapshots are presented in Figure 11 for two energy sources discussed above; the heat fluxes caused by the EMIC

Figure 11

wave energy absorption due to Landau resonance, and the heat fluxes due to Coulomb energy degradation of the RC H^+ and O^+ ions. The energy deposition rates caused by the resonant interaction of the EMIC waves and thermal plasmaspheric electrons are presented in the first and second rows. The (MLT, L–shell) localizations of the energy flux from this channel are practically coincident with the corresponding EMIC wave energy distributions (compare with Figure 6 in paper 1). There are spot–like patches which are mostly localized in the vicinity of the 10^2 cm^{-3} electron number density contour in the plasmasphere boundary layer. The most intense energy deposition rates are observed in the postnoon–premidnight MLT sector, and maximize at the magnitude of $7.8 \cdot 10^{10}$ $(eV/(cm^2 \cdot s)$ at L=3.25, MLT=22 at 34 hours after 1 May, 0000 UT.

The third and fourth rows in Figure 11 are the snapshots of the energy deposition rates into the thermal plasmaspheric electrons due to Coulomb energy degradation of the RC H^+ and O^+ ions. Coulomb collisions occur throughout the plasmasphere–RC overlap region. As a result, this energy source is smooth in intensity, located well earthward of the plasmapause, and spatially separated from the "wave" energy source. Although the intense energy deposition rates are mostly observed in the postnoon–premidnight MLT sector, sometimes this kind of energy source can be effective everywhere encircling almost the entire globe (see, e. g., the hours 40 and 48 in Figure 11). The greatest energy deposition rate of about 10^{11} $(eV/(cm^2 \cdot s)$ is observed at hour 40, and the typical energy deposition rates are about of $2 \cdot 10^{10}$ $(eV/(cm^2 \cdot s)$, and found during two periods; 32–48 hours, and 76–86 hours after 1 May, 0000 UT.

3.2. Electron Heating Events in Subauroral Topside Ionosphere: Qualitative Comparison With Observations

The overlap of the RC with the outer plasmasphere plays a major role in the storm–time related electron temperature elevations in the subauroral topside ionosphere. One of the major deficiencies in the study of the coupling of the RC to the ionosphere is the lack of concurrent and conjugate magnetospheric and ionospheric plasma measurements over complete anomalous heating events. Recently, *Gurgiolo et al.* [2005] have presented a global view of the RC–plasmasphere system during the 18–19 June 2001 storm. In order to have concurrent and conjugate plasma measurements from the plasmasphere, the RC, and the topside ionosphere *Gurgiolo et al.* [2005] have combined data from the IMAGE and DMSP satellites. IMAGE has been used (1) to obtain the plasmaspheric He^+ ion density in the geomagnetic equatorial plane (EUV), and (2) to obtain global 2D distributions of the RC ion fluxes in the geomagnetic equatorial plane (MENA and HENA). DMSP satellites (F–12, F–13, and F–15) have been used to obtain electron temperature and precipitating electron and ion fluxes along the satellite tracks at a nominal altitude of 830 km. *Gurgiolo et al.* [2005] have analyzed the relationships of the topside heating of the subauroral ambient electrons with the plasmasphere and RC conditions. They have found that subauroral heating occurs within the plasmasphere–RC overlap region, and can be separated into two classifications; inner and outer heating events. The inner events take place well earthward of the plasmapause ($> 0.75 R_E$ in the equatorial plane) and generally occur in the dawn MLT sector. The

outer events occur in the plasmasphere boundary layer within $0.75R_E$ of the equatorial plasmapause, and are more prevalent in the dusk MLT sector. Note that sometimes both inner and outer events are observed in the evening MLT sector.

Our theoretical results presented in Figure 11 very clear demonstrate spatial separation between two energy sources for thermal plasmaspheric electrons. The "wave" source produces intense thermal fluxes mainly in the postnoon–premidnight plasmasphere boundary layer, a radially narrow region but extended in MLT. On the other hand, the "Coulomb" source is acting well earthward of the plasmapause and can be found in both postnoon–premidnight and morning MLT sectors. (Although the radial extension of the "Coulomb" source usually exceed $2R_E$ in the postnoon MLT sector, there is less than R_E for the heating radial extension in the dawn MLT sector.) This spatial structure of the thermal electron heating caused by interaction of the RC with the plasmasphere is supported by concurrent and conjugate plasma measurements from the plasmasphere, the RC, and the topside ionosphere [*Gurgiolo et al.,* 2005]. At the same time, we should note that in the present study we do not discuss the mechanisms of energy transfer from the high–altitude energy sources into the ionosphere. (The heat conduction and/or low energy downward electron fluxes are now widely accepted as the main energy transport mechanisms.) So it is not a fact that calculated energy deposition rates are the real thermal fluxes that can be observed at the ionosphere level. These theoretical numbers give only the maximal values of the heat fluxes which could be potentially transfered downward to the ionosphere from the specified energy sources .

The observed heating is mostly localized in the equatorial radial direction (or

in a latitudinal direction as it observed by DMSP satellites), and interpreting the satellite data, *Gurgiolo et al.* [2005] have come to the conclusion that "while Coulomb collisions may act as a heat source in the equatorial plasmasphere, collisional heat conduction is not the source of the heat flux into the ionosphere", and some alternate mechanism(s) should act to transfer the heat into the upper ionosphere. They have tried to explain the observed inner and outer heating events by drawing in the wave instabilities. Although they have had difficulties to explain the heat flux driver for the inner heating events, they convincingly argue that the EMIC wave instability is driving the heat flux into the ionosphere for the outer heating events. This is exactly the result we obtained from our global self–consistent RC–EMIC wave model. Note that there is an extremely important fact we should keep in mind; in spite of the "wave" energy source is less intense globally then the "Coulomb" source, the EMIC waves scatter the thermal electrons into the loss cone (even if these electrons are heating due to Coulomb collisions with RC), so these heated electrons can precipitate into the ionosphere. At the same time, we should emphasize that *Gurgiolo et al.* [2005] have encountered one difficulty connected with employing the EMIC wave instability as a heat driver for the outer heating events. Namely, they have found "in no instance in this entire storm is ion precipitation observed in conjunction with a subauroral temperature enhancement. Ion precipitation is expected to accompany heating produced in the damping of ion cyclotron waves [*Cornwall et al.*, 1971]". We believe that this difficulty can be naturally resolved in the frame of our new RC–EMIC wave theoretical model.

As we have demonstrated in paper 1, the EMIC wave power density distribution

over wave normal angle can occupy not only the region of generation, i. e. the region of small θ_0, but the entire wave normal angle region, and even the region near $\theta_0 = \pi/2$ only. The intensities of the RC ion precipitating fluxes depend on the intensities of the EMIC waves in the region of small θ_0, and the magnitudes of energy deposition rates to thermal electrons mostly depend on the intensities of the oblique EMIC waves. Selecting the same spatial points (a), (b) and (c) as we did in Section 2 analyzing Figures 2 and 3, we list in Table 1 the values for the wave induced energy deposition rates to the thermal plasmaspheric electrons in these points. At point (b), the wave power, $B^2_{\mathrm{w,(b)}}$, has the greatest amplitude, the EMIC wave energy is near evenly distributed in the entire wave normal angle region (see Figure 9(b) in paper 1), and as a result we observe the greatest energy deposition rate in this point. Let us now consider the points (a) and (c). First, for these points the ratio $B^2_{\mathrm{w,(a)}}/B^2_{\mathrm{w,(c)}} = 1.8$ is held. Second, although the core plasma density, n_{e0}, in point (a) is about 30% greater than in point (c), and for the dipole model the ratio of the magnetic fields in these points is $B_{\mathrm{(a)}}/B_{\mathrm{(c)}} = 1.3$ (γ_e depends on n_{e0} and B, see Figure 5), the Landau damping rates are almost the same in these points. So we can expect the energy deposition rate in point (a) to be greater than in point (c). In spite of the above facts, the energy deposition rate in point (a) is more than two times less than in point (c) ($P_{\mathrm{w},e,\mathrm{(a)}}/P_{\mathrm{w},e,\mathrm{(c)}} = 0.4$) because the EMIC wave power spectral density distributions over θ_0 are diametrically opposite in these two points (see Figure 9 in paper 1). As a consequence, we observe the similar intensities of the energy deposition rates in these points, but there is a dramatic difference between the RC proton precipitating fluxes, $J_{lc,\mathrm{(a)}}/J_{lc,\mathrm{(c)}} = 17.7$. So the satellite measurements

[*Gurgiolo et al.,* 2005] and our theoretical results allow us to argue that the subauroral temperature enhancement in the outer heating events (i) is driven by thermal electron energy absorption due to Landau resonance with EMIC waves, and (ii) these events are not necessary to be accompanied by the elevated RC ion precipitations.

3.3. Relationship of Wave Heating to SAR Arcs

In conclusion of this Section, let us point out the possible relation of the Landau resonance between the EMIC waves and thermal plasmaspheric electrons to the energy source to drive excitation of stable auroral red (SAR) arcs. Although the spacecraft and ground–based measurements along with statistical and theoretical studies provide a strong evidence in support of the importance of the Coulomb energy degradation of the RC ions as a SAR arc energy source [*Kozyra et al.,* 1987], the role of plasma waves in SAR arc formation is now unclear and remains a controversial issue [*Kozyra et al.,* 1997b]. The newest SAR arc observations, with instrumentation that allows enhanced spatial and temporal resolution, have revealed surprising spot–like patches of enhanced emissions that move along the length of the SAR arc [*Kozyra et al.,* 1997b]. No explanation for these small–scale structures yet exists. As we demonstrated above, the EMIC waves produce intense electron thermal fluxes in the MLT extended and radially narrow region in the postnoon–premidnight plasmasphere boundary layer. There are spot–like patches of the enhanced heat fluxes, and the most intense energy deposition rate during the studied event reaches the value of 10^{11} $(\mathrm{eV}/(\mathrm{cm}^2 \cdot \mathrm{s})$ at L=3.25, MLT=22 at 34 hours after 1 May, 0000 UT. The first and the second rows in

Figure 12 present the total energy deposition rates caused by the EMIC wave energy absorption and the Coulomb energy degradation of the RC H^+ and O^+ ions. The third and the fourth rows are the heat fluxes due to Coulomb energy degradation of the RC H^+ and O^+ ions only. In many snapshots in this Figure, we can clearly observe the spots of the enhanced energy depositions to thermal electrons. The theoretically obtained great thermal fluxes and their spot–like spatial structure make this "wave" energy source a possible mechanism to drive the above mentioned SAR arc feature. The spot–like spatial structure produced by this "wave" mechanism depends on the structure of the region of enhanced density gradient in the plasmasphere boundary layer, and multiple plasmapause density drops are often observed [*Thorne and Horne,* 1992]. On the other hand, if Coulomb collisions are responsible for the observed spot–like patches of the enhanced heat fluxes, the dense plasma peaks and/or higher density structures in the RC itself are required. Certainly, the additional measurements and theoretical investigations are required in order to explain these small–scale structures in the SAR arcs.

Figure 12

4. Conclusions

In this paper we have continued presentations and discussions of the results of a simulation based on a new global self–consistent theoretical model of interacting RC ions and propagating EMIC waves. This model is a further development of the self–consistent RC–EMIC wave model of *Khazanov et al.* [2002; 2003]. Simulation of the RC dynamics itself in this new model is based on the bounce–averaged kinetic equation, and this

equation is absolutely identical to the corresponding equation in our previous model. But in comparison with the previous RC–EMIC wave model, the modeling of the wave dynamics is essentially different in the present study. In order to describe the EMIC wave evolution we have explicitly included the ray tracing equations in our previous self–consistent model, and have used the complete wave kinetic equation. This is a crucial new feature of the present model and, to the best of our knowledge, ray tracing equations for the first time have been explicitly employed on a global magnetospheric scale in order to describe spatial and temporal evolutions of the RC–EMIC wave system. The differences between the newly developed model and our previous studies [*Khazanov et al.*, 2002; 2003] can be summarized as follows. In the present study (1) the case of multi–species ($e - H^+ - He^+ - O^+$) thermal plasma is considered, (2) wave propagation and refraction is rigorously taken into account in the full wave kinetic equation, (3) there is no wave reflection from the ionosphere, because the He^+–mode is now reflecting from the surfaces of the $O^+ - He^+$ bi–ion hybrid frequency, and in the current study we neglect the tunneling of the waves across the corresponding stop zone (only a minor portion of the EMIC wave energy can tunnel across the reflection region for the adopted O^+ content in the thermal density model, see paper 1 for all details).

In order to study the effects of EMIC wave propagation and refraction on the wave induced RC proton precipitation and heating of the thermal plasmaspheric electrons, we have simulated the May 1998 storm, and have presented the results for two time intervals during the storm. The first interval takes place on 2 May, from 24 hours to 48 hours after 1 May, 0000 UT, and covers the period of first *Dst* dip. The second one

from 72 hours to 86 hours after 1 May, 0000 UT represents the period of largest *Dst* decrease on 4 May. The main findings of paper 2 can be summarized as follows.

1. The wave induced RC proton precipitations have a quite fine structure, and are highly organized by the location of the plasmapause gradient. The strongest fluxes of about $4 \cdot 10^6$ $(\mathrm{cm} \cdot \mathrm{s} \cdot \mathrm{sr})^{-1}$ are observed during the main and early recovery phases of the storm. The very interesting and probably more important finding is that in a number of cases the most intense precipitating fluxes are not simply connected to the most intense EMIC waves. The characteristics of the EMIC wave power spectral density distribution over the wave normal angle is an extremely crucial factor for the effectiveness of the wave induced RC ion scattering.

2. Comparison of the obtained global RC proton precipitating patterns with the results from other ring current model [*Kozyra et al.*, 1997a] reveals that, although we observe a qualitative agreement between localizations of the wave induced precipitations in the models, there is no quantitative agreement between the magnitudes of precipitating fluxes. It has been demonstrated that these differences are mainly due to a qualitative difference between the characters of the EMIC wave power spectral density distributions over the wave normal angle in these two models.

3. Two energy sources for the plasmaspheric thermal electrons are examined; the heat flux caused by the EMIC wave energy absorption due to Landau resonance with electrons, and the heat flux due to Coulomb energy degradation of the RC H^+ and O^+ ions. The (MLT, L–shell) localizations of the energy flux from the "wave" channel are practically coincident with the corresponding EMIC wave energy distributions (compare

Figure 11 with Figure 6 in paper 1). There are spot–like patches which are mostly localized in a vicinity of the 10^2 cm^{-3} electron number density contour, along the most enhanced density gradient in the plasmasphere boundary layer. The heat fluxes caused by the EMIC wave energy absorption are observed in the postnoon–premidnight MLT sector, and maximize at the magnitude of 10^{11} (eV/(cm$^2 \cdot$ s) at L=3.25, MLT=22 at 34 hours after 1 May, 0000 UT. Coulomb collisions occur throughout the plasmasphere–RC overlap region, and as a result this energy source is smooth in intensity, located well earthward of the plasmapause, and spatially separated from the "wave" energy source. The most intense energy deposition rates are observed in the postnoon–premidnight MLT sector, and sometimes this kind of energy source can be effective everywhere encircling almost the entire globe. Although the radial extension of the Coulomb collisional source usually exceeds $2R_E$ in the postnoon MLT sector, there is less than R_E for the heating radial extension in the dawn MLT sector. The greatest Coulomb energy deposition rate of about 10^{11} (eV/(cm$^2 \cdot$ s) is observed at hour 40, and the typical energy deposition rates are about of $2 \cdot 10^{10}$ (eV/(cm$^2 \cdot$ s), and found during two periods; 32–48 hours, and 76–86 hours after 1 May, 0000 UT. The theoretically obtained spatial structure of the thermal electron heating caused by interaction of the RC with plasmasphere is strongly supported by concurrent and conjugate plasma measurements from the plasmasphere, the RC, and the topside ionosphere [*Gurgiolo et al.,* 2005].

4. The SAR arc observations with instrumentation that allows enhanced spatial and temporal resolution, have revealed surprising spot–like patches of enhanced emissions that move along the length of the SAR arc [*Kozyra et al.,* 1997b]. No explanation for

these small–scale structures yet exists. In the present study we have demonstrated that EMIC waves produce intense electron thermal fluxes in the MLT extended and radially narrow region in the postnoon–premidnight plasmasphere boundary layer. There are spot–like patches of the enhanced heat fluxes. Although the additional measurements and theoretical investigations are required, the theoretically obtained great thermal fluxes and their spot–like spatial structure make this "wave" energy source a possible mechanism to drive the observed small–scale structures in the SAR arcs.

Acknowledgments. This research was performed while K. Gamayunov held a NASA Postdoctoral Program appointment at NASA/MSFC. Funding in support of this study was provided by NASA grant UPN 370–16–10. Support for D. Gallagher is provided by the IMAGE Mission through the NASA Science Mission Directorate.

References

Cornwall, J. M., F. V. Coroniti, and R. M. Thorne (1970), Turbulent loss of ring current protons, *J. Geophys. Res., 75,* 4699.

Cornwall, J. M., F. V. Coroniti, and R. M. Thorne (1971), Unified theory of SAR arc formation at the plasmapause, *J. Geophys. Res., 76,* 4428.

Gonzalez, W. D., B. T. Tsurutani, A. L. C. Gonzalez, E. J. Smith, F. Tang, and S.–I. Akasofu (1989), Solar wind–magnetosphere coupling during intense magnetic storms (1978–1979), *J. Geophys. Res., 94,* 8835.

Gurgiolo, C., B. R. Sandel, J. D. Perez, D. G. Mitchell, C. J. Pollock, and B. A. Larsen (2005), Overlap of the plasmasphere and ring current: Relation to subauroral ionospheric heating, *J. Geophys. Res., 110,* A12217, doi:10.1029/2004JA010986.

Jordanova, V. K., C. J. Farrugia, R. M. Thorne, G. V. Khazanov, G. D. Reeves, and M. F. Thomsen (2001), Modeling ring current proton precipitation by EMIC waves during the May 14–16, 1997, storm, *J. Geophys. Res., 106,* 7.

Jordanova, V. K., J. U. Kozyra, A. F. Nagy, and G. V. Khazanov (1997), Kinetic model of the ring current–atmosphere interactions, *J. Geophys. Res., 102,* 14279.

Kennel, C. F., and H. E. Petschek (1966), Limit on stably trapped particle fluxes, *J. Geophys. Res., 71,* 1.

Khazanov, G. V., K. V. Gamayunov, D. L. Gallagher, and J. U. Kozyra (2006), Self–consistent model of magnetospheric ring current and propagating electromagnetic ion cyclotron waves. 1. Waves in multi ion magnetosphere, *J. Geophys. Res.,* in

press.

Khazanov, G. V., K. V. Gamayunov, and V. K. Jordanova (2003), Self–consistent model of magnetospheric ring current ions and electromagnetic ion cyclotron waves: The 2–7 May 1998 storm, *J. Geophys. Res., 108*, A12, 1419, doi:10.1029/2003JA009856.

Khazanov, G. V., K. V. Gamayunov, V. K. Jordanova, and E. N. Krivorutsky (2002), A self–consistent model of the interacting ring current ions and electromagnetic ion cyclotron waves, initial results: Waves and precipitating fluxes, *J. Geophys. Res., 107,* A6, 1085, doi:10.1029/2001JA000180.

Kozyra, J. U., V. K. Jordanova, R. B. Horne, and R. M. Thorne (1997a), Modeling of the contribution of Electromagnetic Ion Cyclotron (EMIC) waves to stromtime ring current erosion, in *Magnetic Storms, Geophys. Monogr. Ser.,* vol. 98, edited by B. T. Tsurutani, W. D. Gonzalez, Y. Kamide, and J. K. Arballo, p. 187, AGU, Washington, D. C..

Kozyra, J. U., A. F. Nagy, and D. W. Slater (1997b), High–altitude energy source(s) for stable auroral red arcs, *Rev. Geophys., 35,* 155.

Kozyra, J. U., E. G. Shelley, R. H. Comfort, L. H. Brace, T. E. Cravens, and A. F. Nagy (1987), The role of ring current O^+ in the formation of stable auroral red arcs, *J. Geophys. Res., 92,* A7, 7487.

Thorne, R. M., and R. B. Horne (1992), The contribution of ion–cyclotron waves to electron heating and SAR–arcs excitation near the storm–time plasmapause, *Geophys. Res. Lett., 19,* 417.

Young, D. T., H. Balsiger, and J. Geiss (1982), Correlations of magnetospheric ion composition with geomagnetic and solar activity, *J. Geophys. Res., 87,* 9077.

D. L. Gallagher, National Space Science and Technology Center, NASA Marshall Space Flight Center, Space Science Department, 320 Sparkman Drive, Huntsville, AL 35805, USA. (e–mail: dennis.l.gallagher@nasa.gov)

K. V. Gamayunov, National Space Science and Technology Center, NASA Marshall Space Flight Center, Space Science Department, 320 Sparkman Drive, Huntsville, AL 35805, USA. (e–mail: konstantin.gamayunov@msfc.nasa.gov)

G. V. Khazanov, National Space Science and Technology Center, NASA Marshall Space Flight Center, Space Science Department, 320 Sparkman Drive, Huntsville, AL 35805, USA. (e–mail: george.khazanov@msfc.nasa.gov)

J. U. Kozyra, Space Physics Research Laboratory, University of Michigan, 2455 Hayward Street, Ann Arbor, MI 49109, USA. (jukozyra@umich.edu)

M. W. Liemohn, Space Physics Research Laboratory, University of Michigan, 2455 Hayward Street, Ann Arbor, MI 49109, USA. (e–mail: liemohn@umich.edu)

Received _____

Figure 1. The RC proton precipitating fluxes averaged over the equatorial pitch–angle loss cone, and integrated over the energy range $1 - 50$ keV. The results are obtained from the model with no wave–particle interaction (basic version of RAM). All specified hours are counted from 0000 UT on 1 May, 1998.

Figure 2. Same as Figure 1, except the complete system of governing equations (21) and (22) from paper 1 is used for the simulation.

Figure 3. Same as Figure 1, except the RC proton precipitating fluxes are obtained from a simulation employing the RAM as it has been described by *Kozyra et al.* [1997a], and *Jordanova et al.* [2001].

Figure 4. The EMIC wave power spectral density asymmetry over the wave normal angle.

Figure 5. The electron Landau damping rates versus the wave normal angle for the He^+–mode of EMIC waves. The plasma is assumed to consist of the Maxwellian electrons, and cold ions (77% of H^+, 20% of He^+, and 3% of O^+). The second row in the figure represents the corresponding results from the first row but in the vicinity on the damping rate maximum only. All the results are calculated for the wave frequency $\nu = \omega/2\pi = 0.286$ Hz. (a,b) The electron number density and magnetic field are taken from our global model at location L=5.75, MLT=14, at 48 hours after 1 May 1998, 0000 UT (nominal case). (c,d) The doubled electron number density of the nominal case. (e,f) The one and half of the magnetic field amplitude of the nominal case.

Figure 6. Fractions of the RC ions at geosynchronous distance for the May 2–7, 1998 storm period.

Figure 7. Coulomb collisional energy deposition rate (EDR) to the thermal electrons at the topside ionospheric altitude due to interaction with the RC H^+ ions. All the heat fluxes are mapped back in the equatorial plane along the dipole field lines. The first, second, and third rows represent the results for the electron temperature of 0.5, 1.0, and 2.0 eV, respectively. The hours are counted from 0000 UT on 1 May, 1998.

Figure 8. Same as Figure 7, except for the RC O^+ ions.

Figure 9. Energy dependence of the Coulomb collisional energy loss per unit length (arbitrary units) experienced by the RC ions in a specified background plasma, G. All the results are presented for the constant plasma characteristics except electron temperature (0.5, 1, and 2 eV). (a) The energetic ion is H^+ ion, and (b) the energetic ion is O^+ ion. Two vertical lines restrict the typical energy range of maximum RC fluxes.

Figure 10. Coulomb collisional energy deposition rates to the thermal plasmaspheric electrons at the topside ionospheric altitude due to interaction with the RC O^+ and H^+ ions. All the heat fluxes are obtained for $T_e = 1$ eV, and are mapped back in the equatorial plane along the dipole field lines. The first and second rows represent the O^+ energy source, and the third and fourth rows represent the energy source resulting from the RC H^+, respectively. The white lines are the contours of equatorial plasmaspheric electron density, and all specified hours are counted from 0000 UT on 1 May, 1998.

Figure 11. Energy deposition rates to the thermal plasmaspheric electrons at the topside ionospheric altitude. All the heat fluxes are obtained for $T_e = 1$ eV, and are mapped back in the equatorial plane along the dipole field lines. The first and second rows show the deposition rates caused by the EMIC wave energy absorption due to Landau resonance with thermal electrons. The third and fourth rows are the heat fluxes due to Coulomb energy degradation of the RC H^+ and O^+ ions. White lines show the contours of equatorial plasmaspheric electron density, and as everywhere all specified hours are counted from 0000 UT on 1 May, 1998.

Figure 12. Energy deposition rates to the thermal plasmaspheric electrons at the topside ionospheric altitude. All the heat fluxes are obtained for $T_e = 1$ eV, and are mapped back in the equatorial plane along the dipole field lines. The first and second rows show the total deposition rates caused by the EMIC wave energy absorption and the Coulomb energy degradation of the RC H^+ and O^+ ions. The third and fourth rows are the heat fluxes due to Coulomb energy degradation of the RC H^+ and O^+ ions only. All the specified hours are counted from 0000 UT on 1 May, 1998.

Table 1. Wave induced RC proton precipitating fluxes, the equatorial EMIC wave power densities, and the "wave" energy deposition rates to thermal plasmaspheric electrons.

Point Coordinates	Our Model			RAM, *Kozyra et al.* [1997a]	
	J_{lc}	B_{w}^2	$P_{\mathrm{w},e}$	J_{lc}	B_{w}^2
	$(\mathrm{cm}\cdot\mathrm{s}\cdot\mathrm{sr})^{-1}$	nT^2	$\mathrm{eV}/(\mathrm{cm}^2\cdot\mathrm{s})$	$(\mathrm{cm}\cdot\mathrm{s}\cdot\mathrm{sr})^{-1}$	nT^2
(a) L=5.25, MLT=16	$2.5\cdot10^6$	28.6	$4.8\cdot10^9$	$2.7\cdot10^5$	0.2
(b) L=5.75, MLT=15	$1.1\cdot10^6$	41.6	$2.0\cdot10^{10}$	$4.1\cdot10^6$	0.7
(c) L=5.75, MLT=14	$1.4\cdot10^5$	16.3	$1.2\cdot10^{10}$	$2.2\cdot10^6$	0.7

May 2–7, 1998 Magnetic Storm
Ion Fluxes, No Waves: 1 – 50 keV

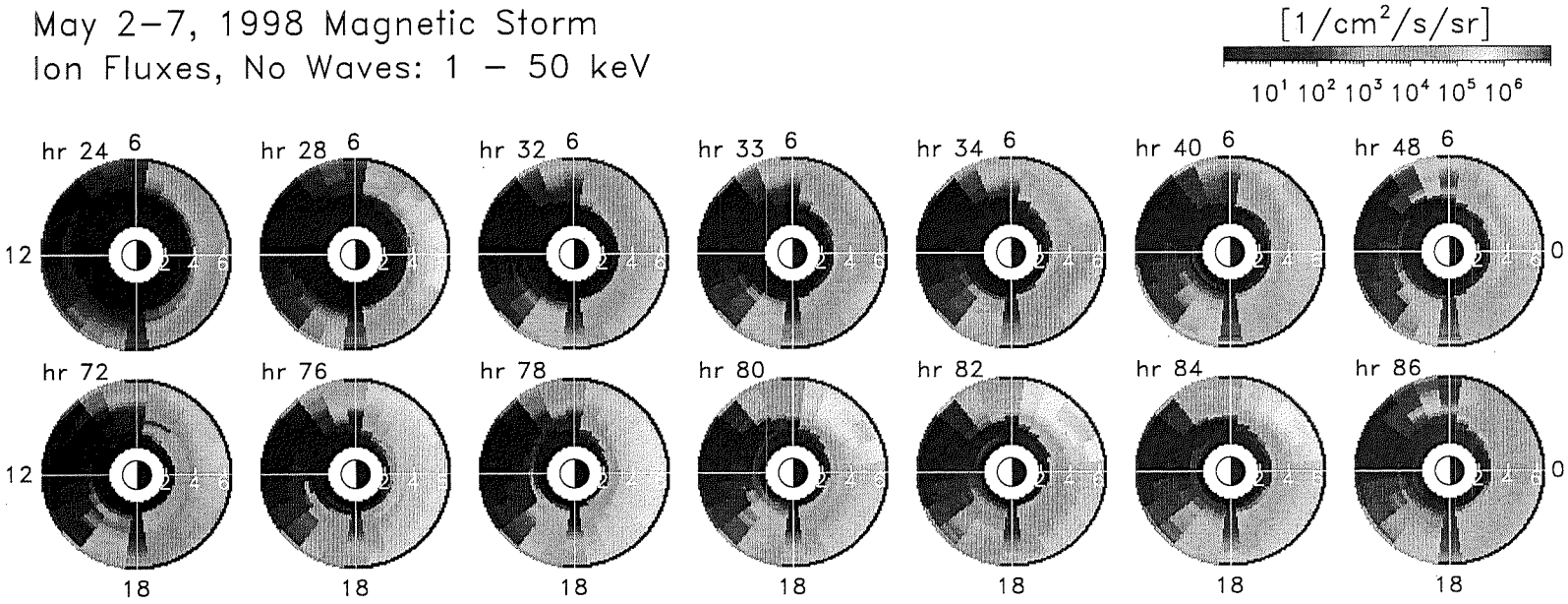

May 2–7, 1998 Magnetic Storm
Ion Fluxes, With Ray Tracing: 1 – 50 keV

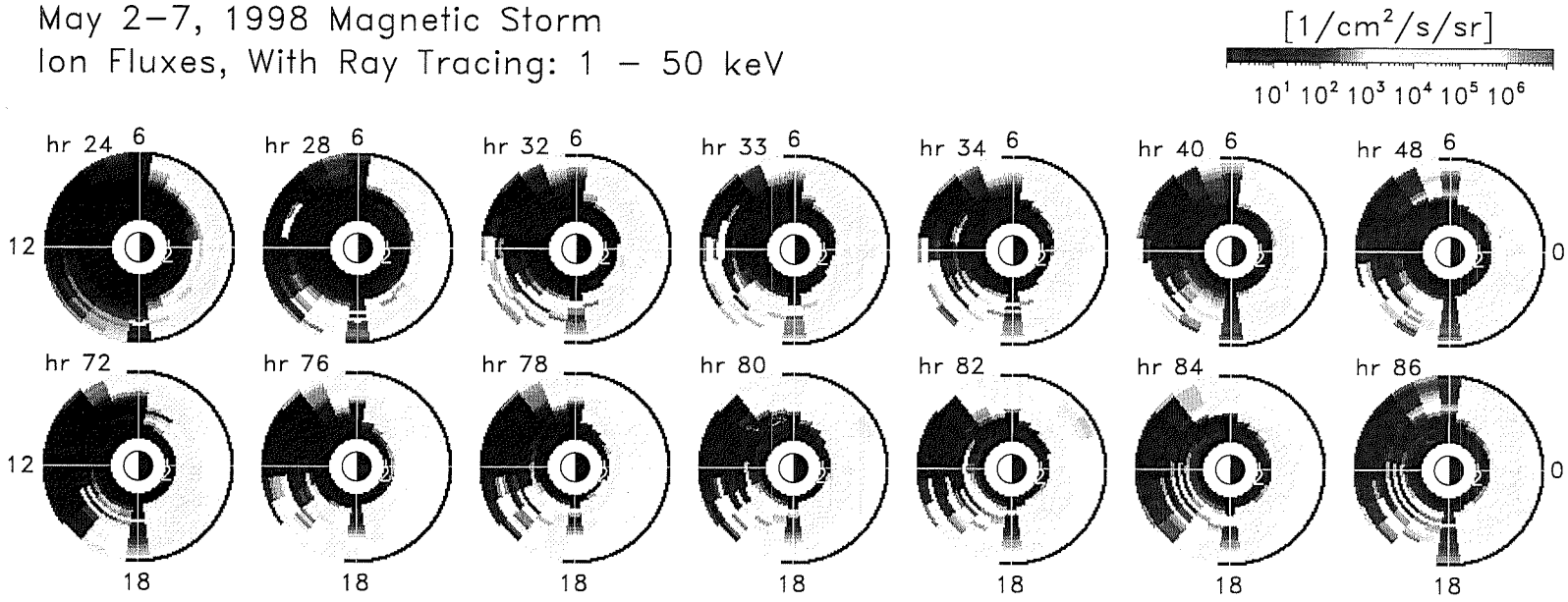

May 2–7, 1998 Magnetic Storm
Ion Fluxes, RAM Model: 1 – 50 keV

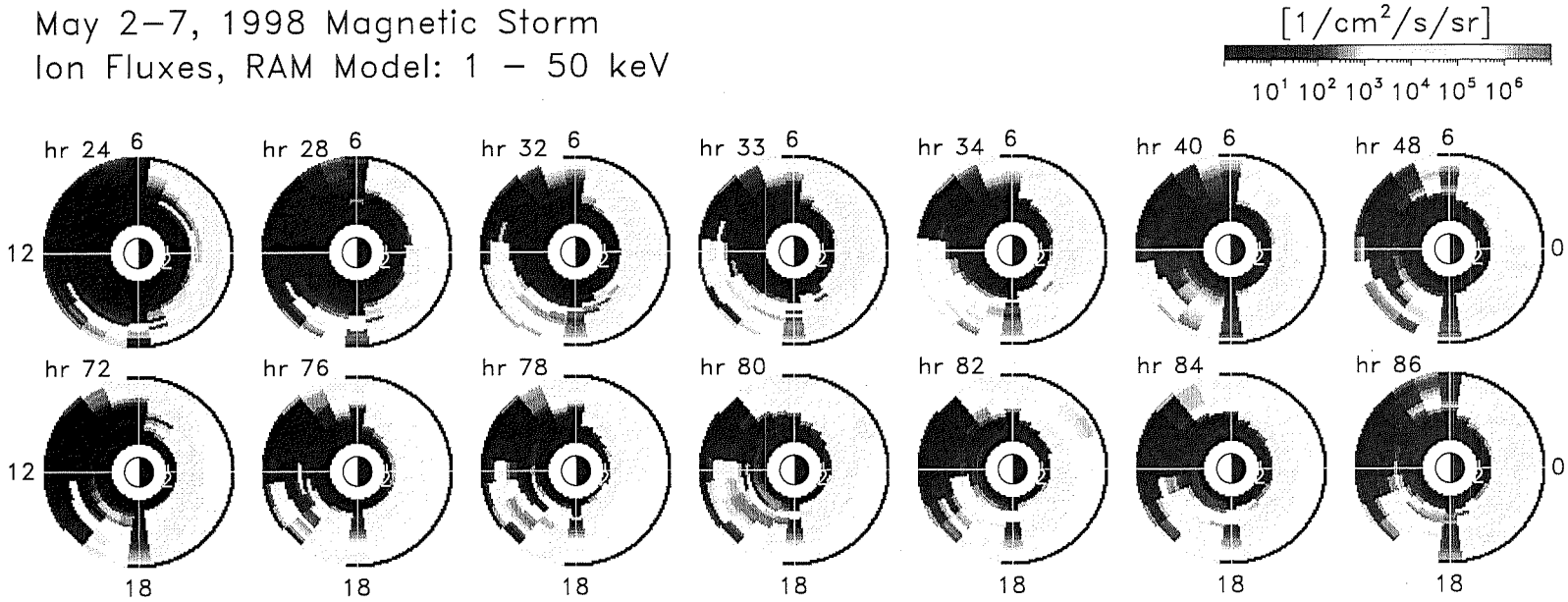

May 2–7, 1998 Magnetic Storm

$(B^2_{45°-90°} - B^2_{0°-45°}) / (B^2_{45°-90°} + B^2_{0°-45°})$

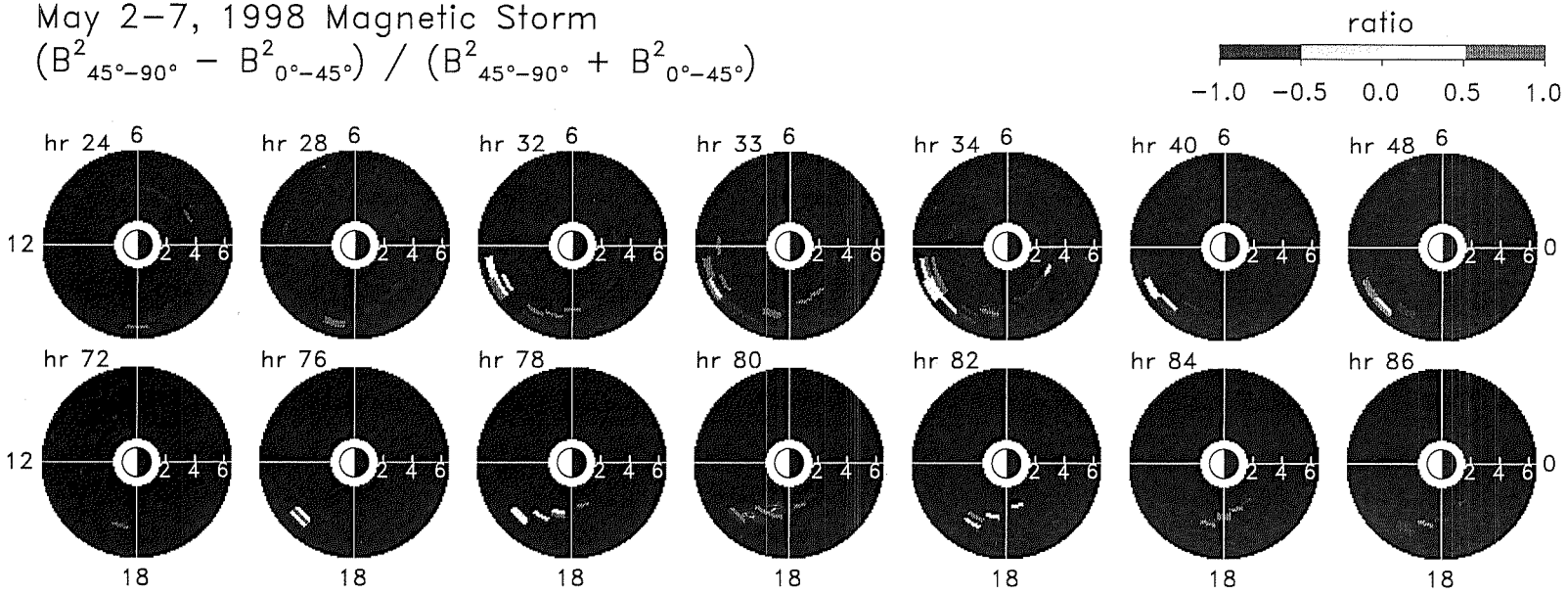

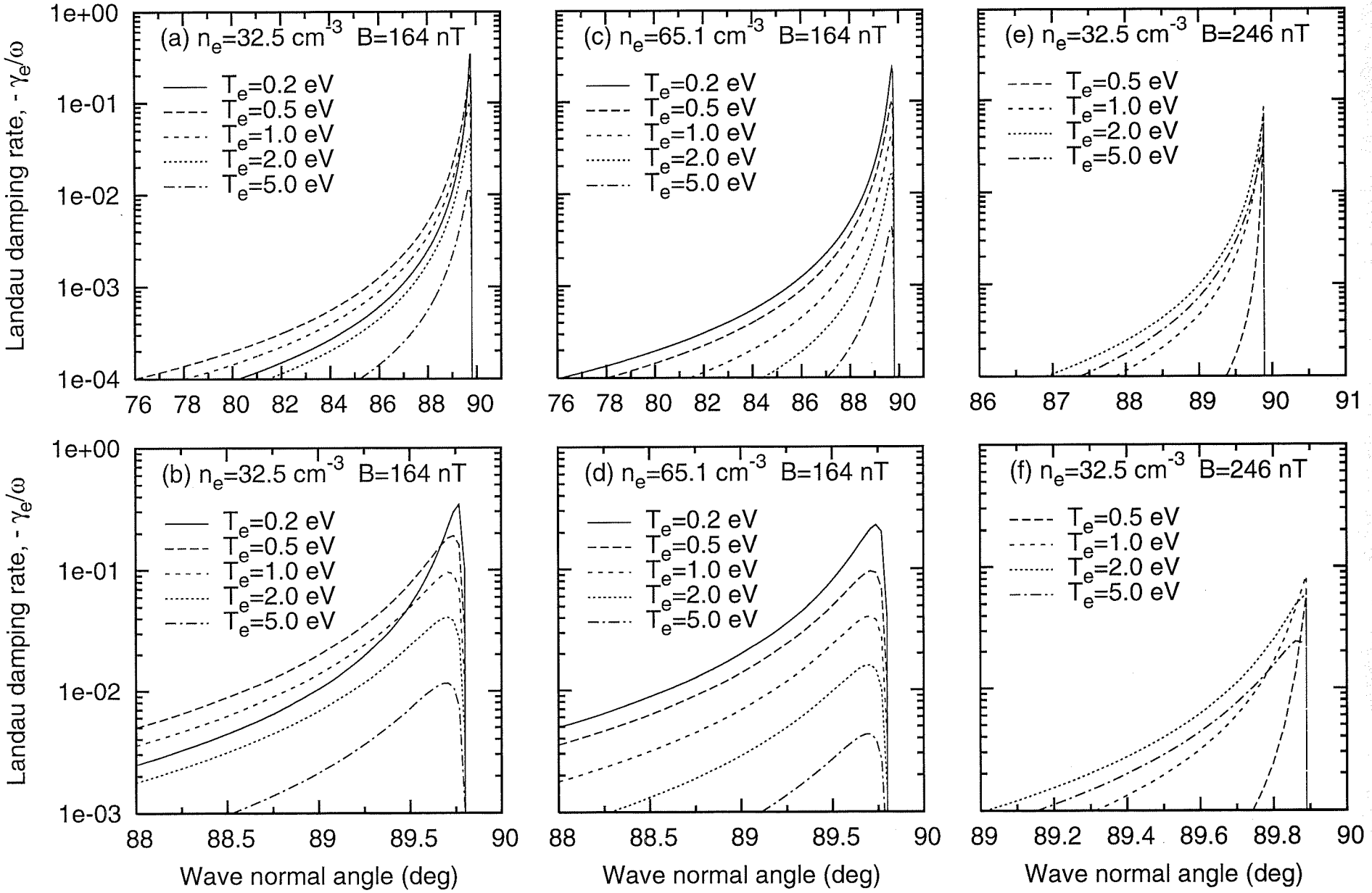
(a) n_e=32.5 cm^{-3} B=164 nT
(b) n_e=32.5 cm^{-3} B=164 nT
(c) n_e=65.1 cm^{-3} B=164 nT
(d) n_e=65.1 cm^{-3} B=164 nT
(e) n_e=32.5 cm^{-3} B=246 nT
(f) n_e=32.5 cm^{-3} B=246 nT
T_e=0.2 eV
T_e=0.5 eV
T_e=1.0 eV
T_e=2.0 eV
T_e=5.0 eV
Landau damping rate, - γ_e/ω
Wave normal angle (deg)

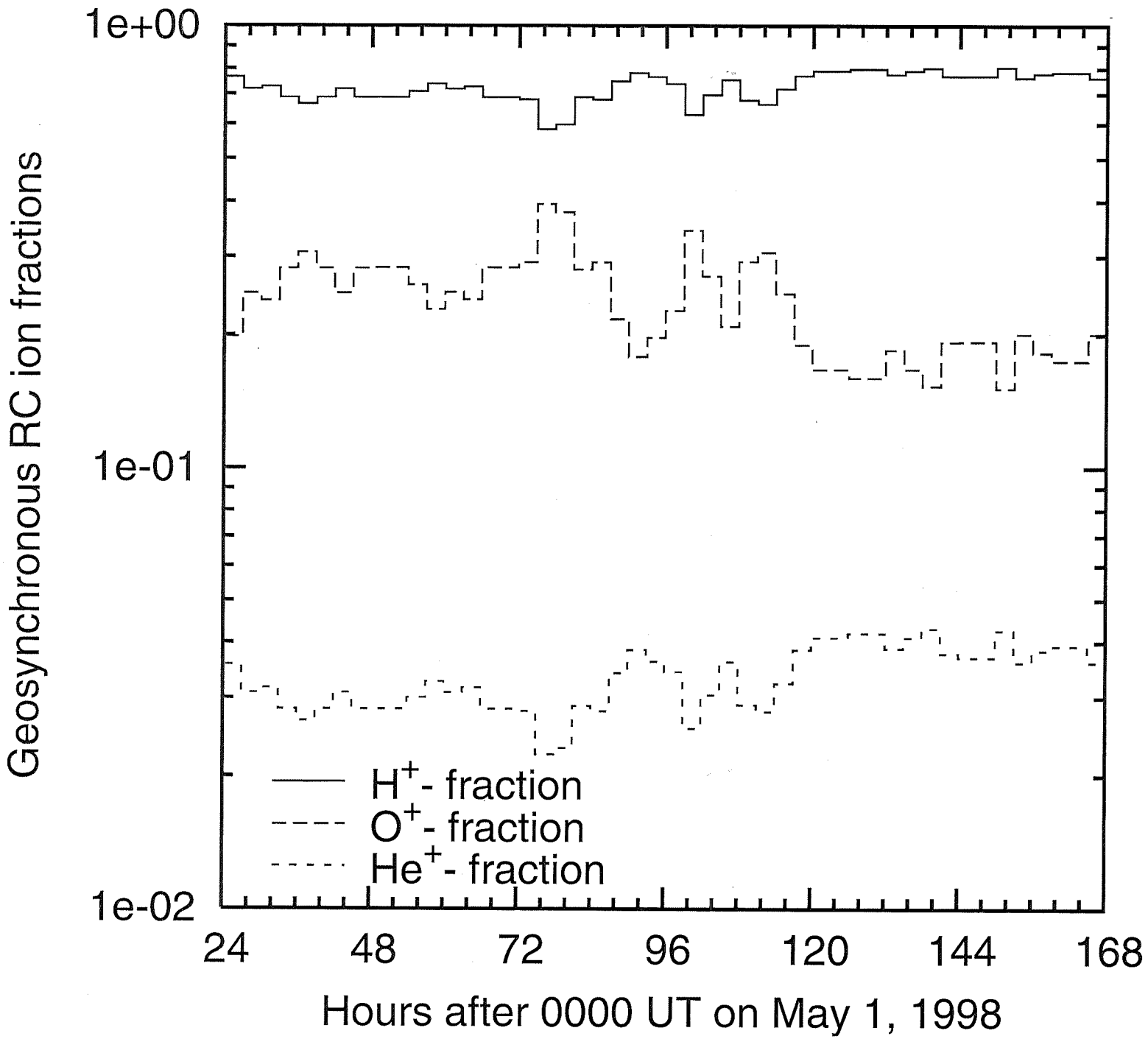
1e+00
1e-01
1e-02
Geosynchronous RC ion fractions
H+- fraction
O+- fraction
He+- fraction
24
48
72
96
120
144
168
Hours after 0000 UT on May 1, 1998

May 2–7, 1998 Magnetic Storm
RC H^+ CC EDR to Electrons (0.5eV, 1eV, 2eV)

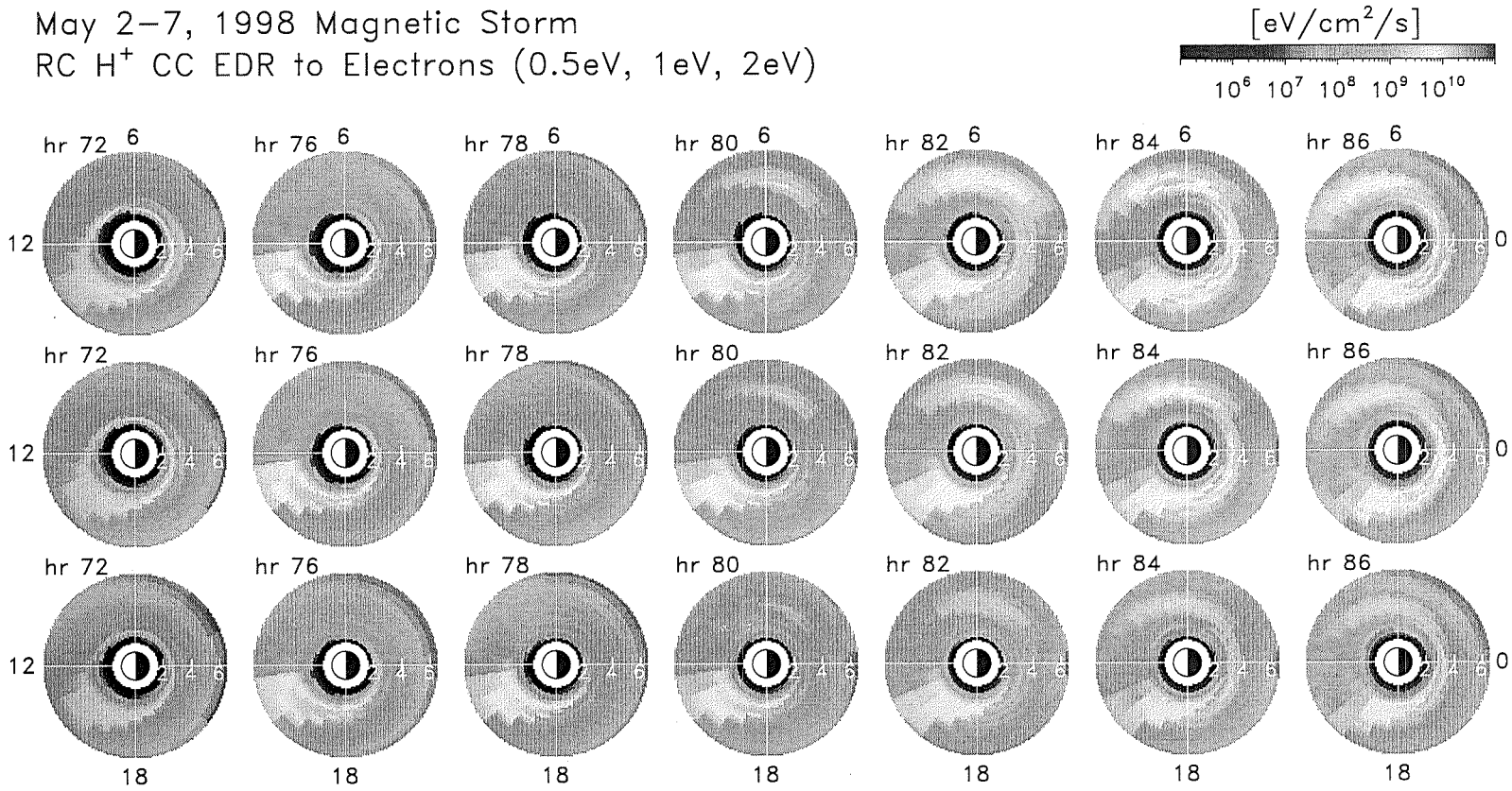

May 2–7, 1998 Magnetic Storm
RC O^+ CC EDR to Electrons (0.5eV, 1eV, 2eV)

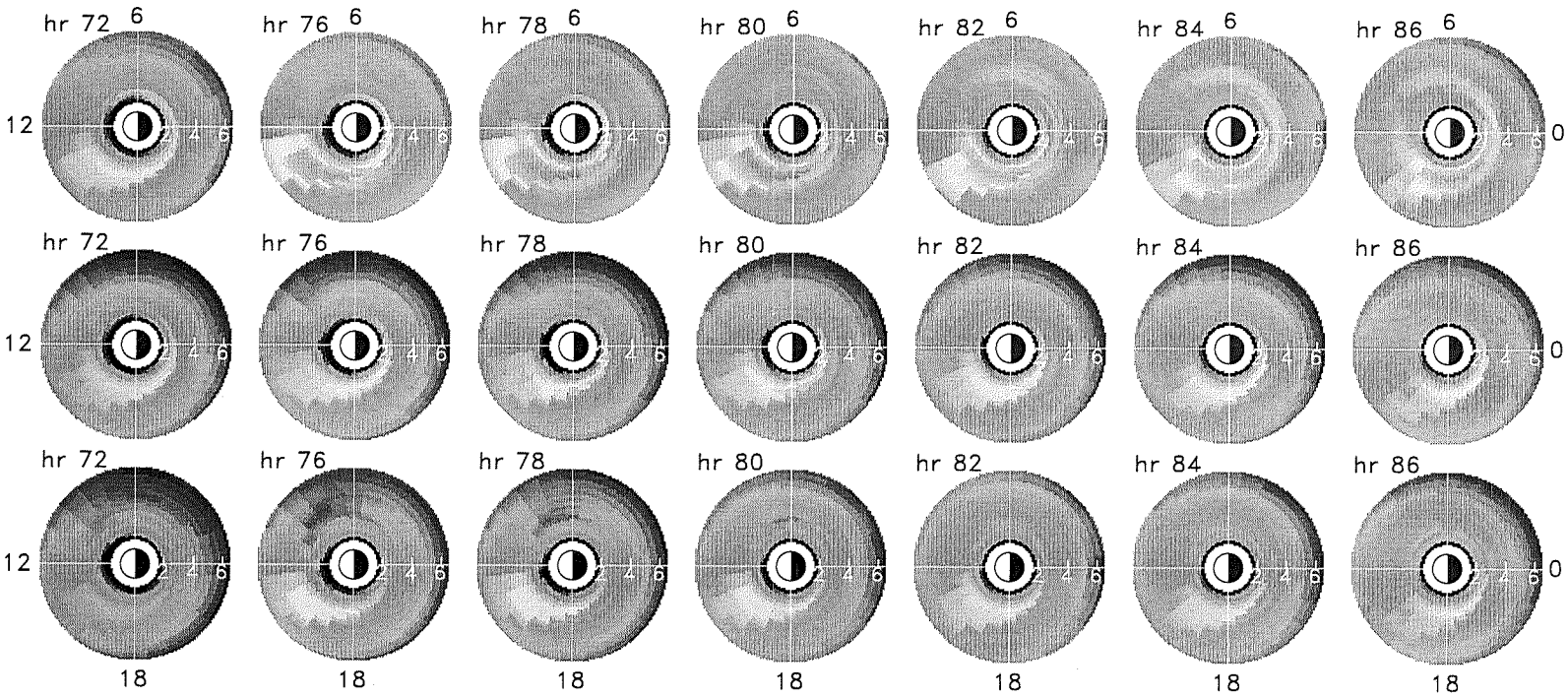

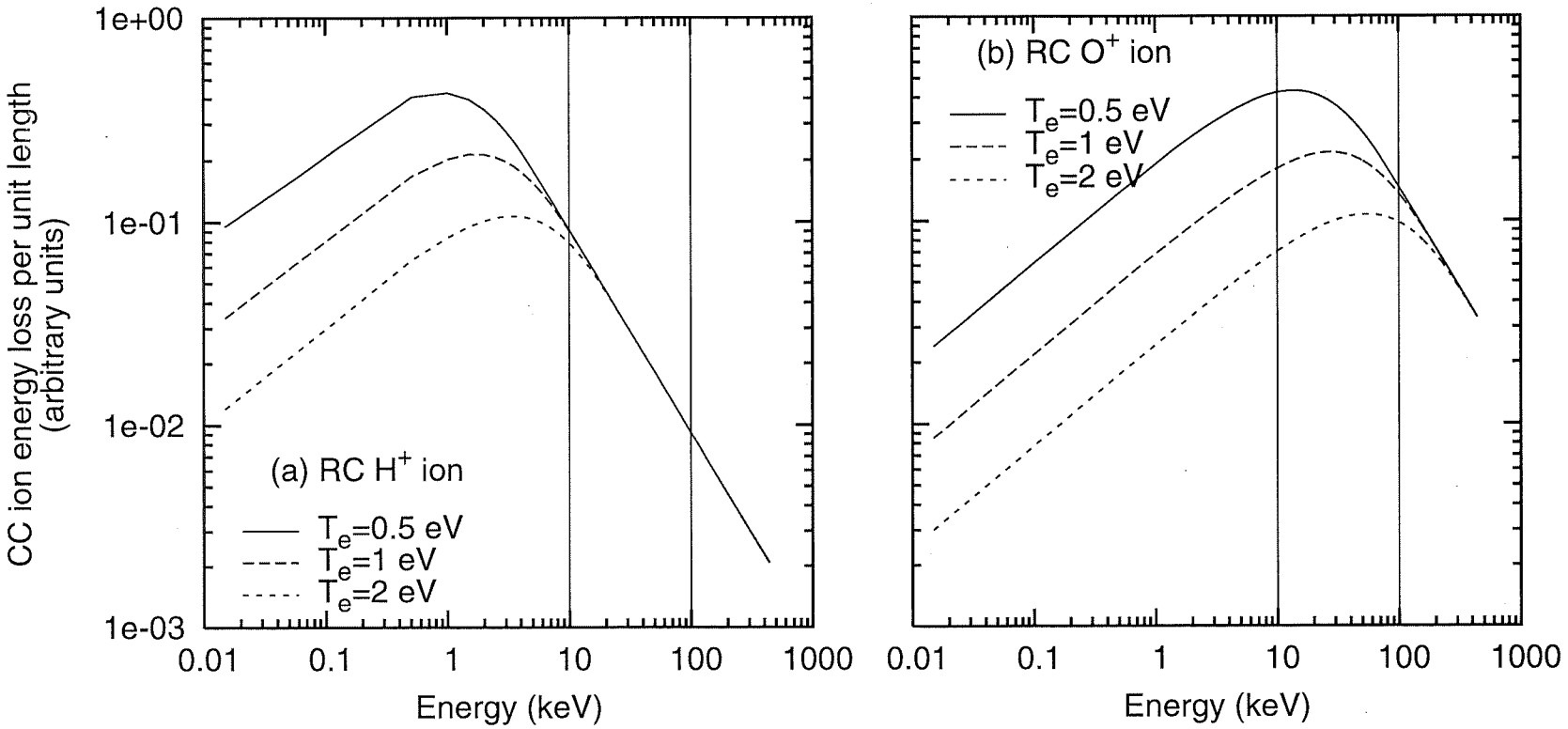
CC ion energy loss per unit length
(arbitrary units)
1e+00
1e-01
1e-02
1e-03
0.01
0.1
1
10
100
1000
Energy (keV)
(a) RC H+ ion
Te=0.5 eV
Te=1 eV
Te=2 eV
(b) RC O+ ion
Te=0.5 eV
Te=1 eV
Te=2 eV
0.01
0.1
1
10
100
1000
Energy (keV)

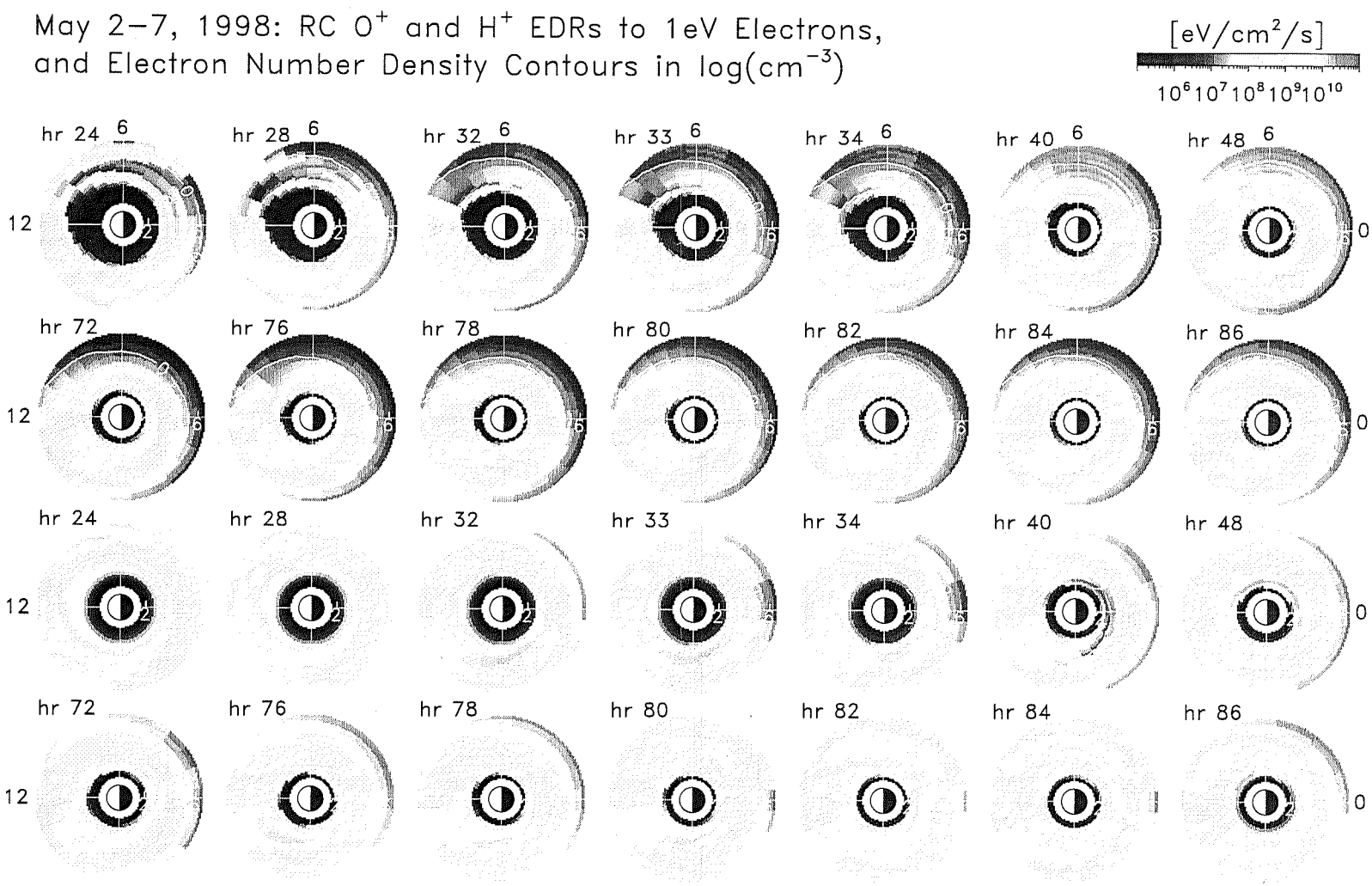
May 2–7, 1998: RC O+ and H+ EDRs to 1eV Electrons,
and Electron Number Density Contours in log(cm-3)
[eV/cm2/s]
10^6 10^7 10^8 10^9 10^10
hr 24
hr 28
hr 32
hr 33
hr 34
hr 40
hr 48
hr 72
hr 76
hr 78
hr 80
hr 82
hr 84
hr 86
12
0
6
2

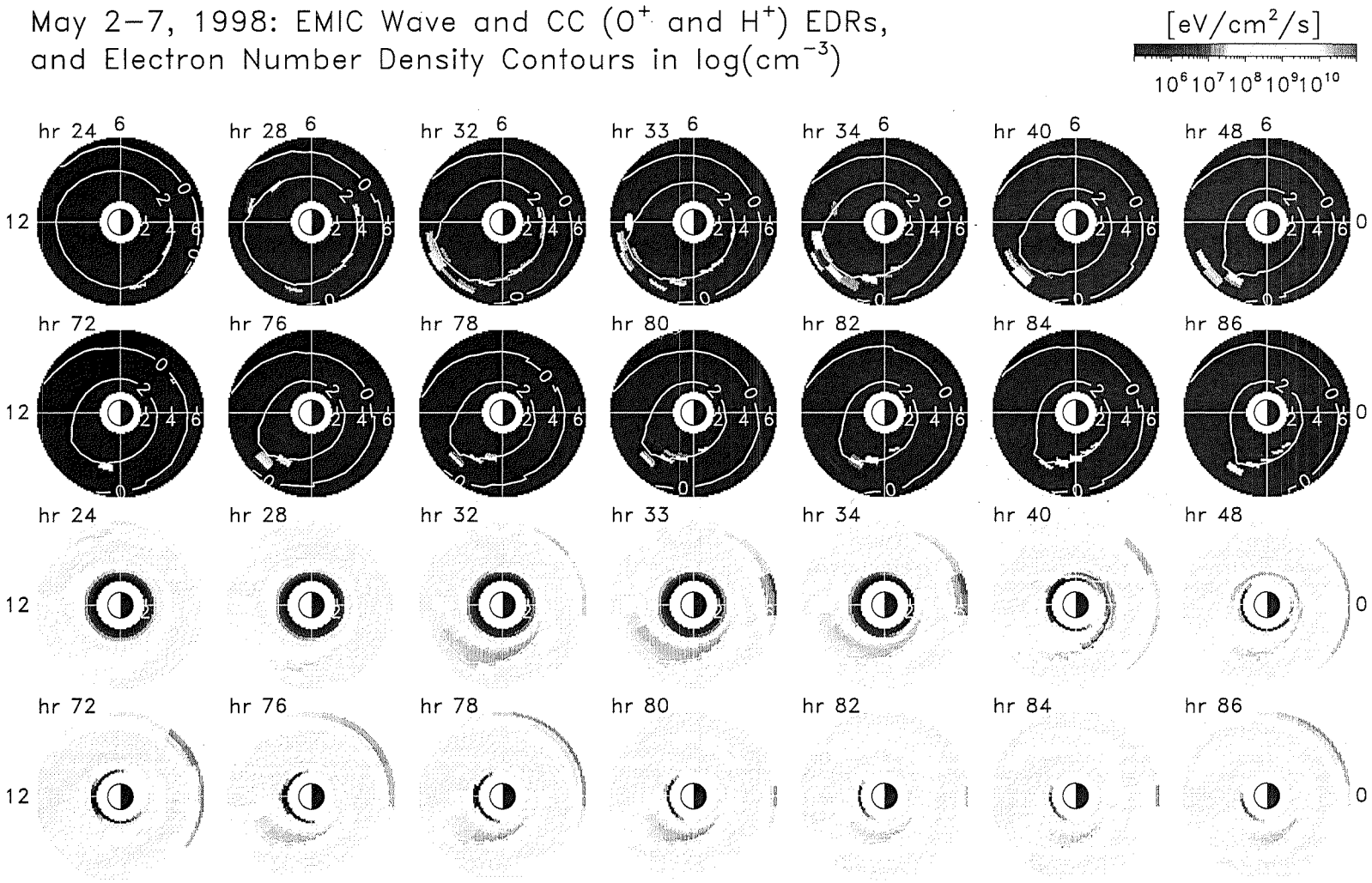
May 2–7, 1998: EMIC Wave and CC (O^+ and H^+) EDRs,
and Electron Number Density Contours in log(cm^{-3})
[eV/cm²/s]
10^6 10^7 10^8 10^9 10^{10}
hr 24
hr 28
hr 32
hr 33
hr 34
hr 40
hr 48
hr 72
hr 76
hr 78
hr 80
hr 82
hr 84
hr 86
6
12
0

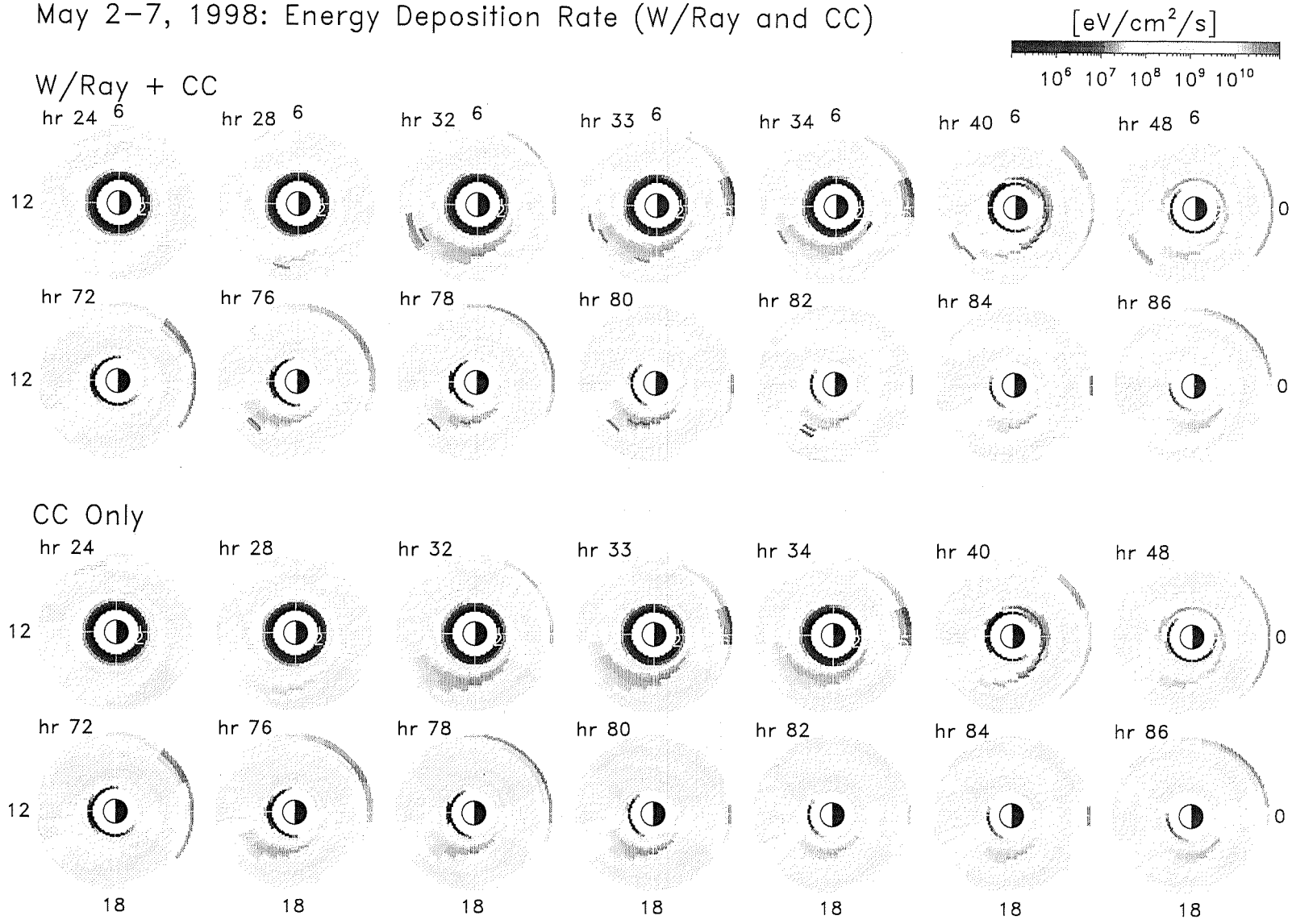
May 2–7, 1998: Energy Deposition Rate (W/Ray and CC)
[eV/cm²/s]
10⁶ 10⁷ 10⁸ 10⁹ 10¹⁰
W/Ray + CC
hr 24
hr 28
hr 32
hr 33
hr 34
hr 40
hr 48
hr 72
hr 76
hr 78
hr 80
hr 82
hr 84
hr 86
CC Only
hr 24
hr 28
hr 32
hr 33
hr 34
hr 40
hr 48
hr 72
hr 76
hr 78
hr 80
hr 82
hr 84
hr 86
6
12
0
18